Catalysis Letters
https://doi.org/10.1007/s10562-021-03726-1

A Stable Zinc Zeolite Catalyst for Dehydrogenation of Ethane to Aromatics and Ethylene

Baocheng Qiu[1] · **Yakun Zhang**[1] · **Yi Zhang**[1]

Received: 2 June 2021 / Accepted: 30 June 2021

Abstract

The rapid deactivation caused by coke deposits is the major obstacle to the ethane aromatization of Zn-based catalysts. We have successfully synthesized a Zn-embedded inside HZSM-5 crystal catalyst (Zn@HZSM-5) by hydrothermal synthesis using preformed Zn/SiO_2 as the only silicone source. Based on various characterization results, including in situ etching XPS, operando DRIFTS, as well as NMR, it is found that $Zn(OH)^+$ and $[Zn–O–Zn]^{2+}$ species are active sites for ethane aromatization for zinc-based catalysts, and their dynamic transformation significantly changes reaction performance of ethane dehydrogenation. For the Zn/HZSM-5 catalyst, the existence of a large number of $[Zn–O–Zn]^{2+}$ species causes higher initial ethane conversion and higher selectivity of aromatics, resulting in a large amount of coke deposits. Moreover, $[Zn–O–Zn]^{2+}$ species on the Zn/HZSM-5 catalyst fast transit to $Zn(OH)^+$ species and subsequently form the sintered ZnO species, leading to rapid deactivation. For the Zn@HZSM-5 catalyst, the embedded structure contributes to forming more $Zn(OH)^+$ species and delays the transformation of the $Zn(OH)^+$ species to $[Zn–O–Zn]^{2+}$ species, resulting in slowly increased selectivity of aromatics during the reaction. Therefore, the Zn@HZSM-5 catalyst realizes stable ethane conversion with dynamic selectivity.

Graphic Abstract

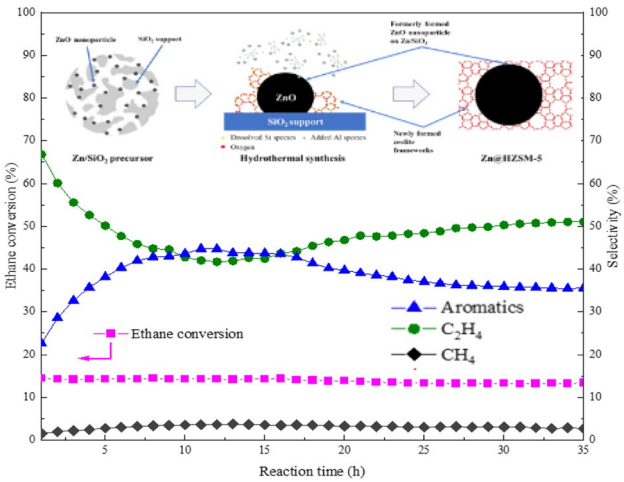

Keywords Ethane · Embedment structure · Zn species · ZSM-5 · Dehydrogenation

1 Introduction

As the second component of shale gas, there is on-growing attention on the effective use of ethane with the global shale gas revolution. The conversion of shale-based cheap ethane

✉ Yi Zhang
yizhang@mail.buct.edu.cn

[1] College of Chemical Engineering, Beijing University of Chemical Technology, 15 Beisanhuan East Road, Beijing 100029, China

Published online: 08 July 2021

to chemicals would decrease the utilization of petroleum and contribute to reduction of carbon emission. One of the most promising pathways is the conversion of ethane to aromatics and ethylene through a dehydrogenation reaction, and those are the building-block chemicals in the petrochemical industry.

For the aromatization of light alkanes, including ethane, many researchers use HZSM-5 zeolite to support metal cations or oxides, including Zn, Re, Pt, Ga, Mo to form aromatics due to its acidic sites and excellent shape selectivity to aromatics [1, 2]. Among these active metals, the zinc-based catalyst is one of the most hopeful catalysts due to its price advantage and high catalytic performance in the alkane aromatization reaction. It has been broadly accepted that the unique catalytic property of the Zn-based HZSM-5 catalyst comes from the combination of zinc species and HZSM-5 [3, 4]. Although various theoretical [5, 6] and experimental [7–9] studies have focused on the active sites and catalytic dehydrogenation mechanisms of light alkanes on the Zn-based HZSM-5 catalyst, the nature of Zn species and the corresponding alkanes activation mechanisms are still being disputed.

Generally, the Zn species in Zn-based HZSM-5 usually contain isolated Zn^{2+} ions, $[Zn–O–Zn]^{2+}$, and bulky intra-zeolite or extra-zeolite clusters of zinc oxide [7, 10, 11]. The isolated Zn^{2+} ions species combined with acidic sites of HZSM-5 and stabilized at the cation-exchange sites of the zeolite, including $(O–Zn^{2+}–O)$ and $Zn(OH)^+$ species [12]. The binuclear $[Zn–O–Zn]^{2+}$ species were formed by condensation of two $Zn(OH)^+$ species. Liu et al. found that the $[Zn–O–Zn]^{2+}$ species are more active in activating the C–H bond of short-chain alkanes than the other zinc species [13, 14]. However, the recombination and desorption of H atoms on $[Zn–O–Zn]^{2+}$ are difficult, which will lead to the formation of methane [15]. Berndt et al. proposed that $Zn(OH)^+$ species exist in Zn/ZSM-5, and its catalytic activity is associated with the content of $Zn(OH)^+$ in the aromatization of propane [16, 17]. Similarly, Niu et al. suggested that $Zn(OH)^+$ species play a significant role in improving the dehydrogenation of alkanes and the aromatization of alkenes [10]. On the contrary, Biscardi et al. believed that the $Zn(OH)^+$ species was unstable, which would further react with acidic OH groups to form active $(O–Zn^{2+}–O)$ species in propane aromatization [4]. Therefore, the true active sites of zinc-based catalysts still need to be discovered.

For Zn-based HZSM-5 catalysts prepared by the conventional method, due to the high temperature and atmospheric pressure are thermodynamically favorable for coke formation during the reaction, the most urgent problem is the rapid deactivation caused by coke deposits [18]. Those cokes not only block micropores but also cover Zn species, which makes it hard for us to investigate the true effects of the active Zn species in ethane aromatization [19]. Many approaches have been taken to diminish coke formation for ethane aromatization and improve the stability. Mehdad et al. used the steam and CO_2 to improve catalyst lifetime and remove a fraction of the coke [20]. However, the aromatics selectivity is less than 10.0%, and the selectivity of CO is more than 30.0%. Steinberg et al. added the H_2 in ethane to promote faster hydrogenation/decomposition of coke precursors. Nevertheless, the yield of CH_4 increased to ~ 11.0 wt%, and the yield of ethylene and total aromatics at 600 °C decreased to ~ 1.5 wt% and ~ 4.0 wt%, respectively [21].

Although the above methods can delay the catalyst deactivation to some extent, the poor stability of the catalyst due to coke deposits still exists, which makes it difficult for us to investigate Zn species during the reaction. Furthermore, the zinc species of Zn-based catalysts prepared by conventional methods are easily transformed during the reaction, including the location and particle size of zinc species, those would further increase the complexity and difficulty of clarifying the role and state of zinc species [3]. Herein, we explored the possibility of embedding Zn particles into the HZSM-5 crystal through a two-step crystallization process using Zn/SiO_2 as the precursor and consequently obtained the embedded Zn@HZSM-5 catalyst with a stable active Zn species, which has a unique combination with acidic sites in HZSM-5. In order to investigate the state of Zn species, all prepared catalysts were tested in ethane dehydrogenation and carefully characterized by many methods, including in-situ XPS, operando DRIFTS, and NMR.

2 Experimental Sections

2.1 Reagents and Materials

Silica gel I with SSA (Specific surface area) of 480 m^2/g was purchased from Shanghai Aladdin Biochemical Technology Co., Ltd. The TPAOH (Tetrapropyl ammonium hydroxide, 25.0% aqueous solution) was bought from Shanghai Macklin Biochemical Co., Ltd. The absolute ethanol (99.5%), $NH_3·H_2O$ (40.0% aqueous solution), $Zn(CH_3COO)_2$ (AR), and $Al(NO_3)_3·9H_2O$ (AR) were purchased from Beijing Tongguang Fine Chemical Company. The high purity N_2 (99.999%), Feed gas (C_2H_6/N_2, 9/1, v/v), and Air were supported by Beijing AP BAIF Gases Industry Co., Ltd. The commercial HZSM-5 (Si/Al = 20) was purchased from Nankai University Catalyst Company. The chemicals involved in this study were used without further purification.

2.2 Synthesis of the Embedded Zn@HZSM-5 Zeolite Catalyst

2.2.1 Preparation of Precursor Catalyst Zn/SiO_2

The precursor Zn/SiO_2 was prepared by the IWI (Incipient wetness impregnation) method from our former work [22]. The Silica gel I and $Zn(CH_3COO)_2$ were used as the support and the zinc source of precursor, respectively. The Zn/SiO_2 with a nominal 3 wt% zinc loading was prepared by impregnation of the SiO_2 (3.0 g) with an aqueous solution (3.18 g) containing 0.32 g of $Zn(CH_3COO)_2$. Then the sample was vacuumed for 1 h in a vacuum container, after that, the sample was dried in a drying oven at 120 °C for 12 h, and finally placed in a muffle furnace at 400 °C for 2 h. The resulting sample is denoted as Zn/SiO_2.

2.2.2 Synthesis of Zn@HZSM-5 Zeolite

Zn@HZSM-5 zeolite (Si/Al = 20) was prepared by a two-step synthesis method. Typically, an aqueous solution (3.19 g) containing 0.47 g of $Al(NO_3)_3{\cdot}9H_2O$ was impregnated by the IWI method into the precursor Zn/SiO_2. Then, the sample was dried at 120 °C for 12 h to remove excess moisture. Subsequently, 3.19 g of TPAOH solution was impregnated into the above sample by the IWI method. Then put it into a vacuum container and vacuum for 0.5 h, followed by transferring into a Teflon-lined autoclave and kept for 31 h at 180 °C. After the autoclave was cooled to room temperature, the sample was taken out and dried at 120 °C for 12 h and then ground to below 100 mesh.

After that, EtOH, $Al(NO_3)_3{\cdot}9H_2O$, the pre-crystallized sample, TPAOH, $NH_3{\cdot}H_2O$ were well dissolved in deionized water in order with a molar ratio of Si: Al: TPAOH: NH_3: EtOH: H_2O = 1: 0.025: 0.375: 5: 12.5: 40. Specifically, 28.76 g of ethanol was poured into a Teflon liner and stirred, and then 11.60 g of an aqueous solution with 0.47 g of $Al(NO_3)_3{\cdot}9H_2O$ was added dropwise to the liner. After that, the pre-crystallized sample (below 100 mesh) was put into the liner and stirred, then 15.20 g of TPAOH was added dropwise and stirred for 30 min, and finally 17.0 g of $NH_3{\cdot}H_2O$ was added dropwise and stirred for 10 min. Eventually, the mixture solution was transferred into a Teflon-lined autoclave and kept for 48 h at 180 °C. After the autoclave was cooled to room temperature, the product was isolated by filtration and washed several times with deionized water and ethanol. The resulting product was dried at 120 °C for 12 h and then calcined at 550 °C (heating rate, 2 °C/min) for 6 h, and finally obtained Zn-embedded HZSM-5 zeolite, which is denoted as Zn@HZSM-5 in this article.

2.3 Preparation of Zeolite-Supported Catalyst Zn/HZSM-5

For comparison, the Zn/HZSM-5 was prepared by the conventional impregnation method using the commercial HZSM-5 as support. Before preparing the catalyst, commercial HZSM-5 zeolite (Si/Al = 20) was calcined in air at 550 °C for 2 h to remove moisture and impurities. Specifically, the 3.0 g of commercial HZSM-5 (Si/Al = 20) was impregnated with an excessive aqueous solution prepared by dissolving 0.32 g of $Zn(CH_3COO)_2$ in 10 g deionized water. Subsequently, the sample was stirred on a magnetic stirrer at 60 °C until the water had evaporated. Then, the mixture was dried in a 120 °C drying oven for 12 h and calcined in a 400 °C muffle furnace for 2 h. Finally, the obtained sample was named Zn/HZSM-5.

2.4 Ethane Aromatization Reaction

Catalytic evaluations of Zn@HZSM-5 and Zn/HZSM-5 catalysts were conducted in a fixed-bed reactor. Generally, 0.30 g of sample was loaded into a quartz tube reactor with an inner diameter of 8 mm. Before the experiment, the sample was heated in an Air flow (20 ml/min) at 200 °C for 30 min to remove the moisture. The feed gas is a high-concentration ethane (C_2H_6/N_2, 9/1, v/v) gas. All transfer lines were kept at 150 °C to prevent condensation of heavy aromatic products.

2.5 Products Analysis

The effluent gases were periodically analyzed by two on-line Shimadzu GC-2014C with one TCD (Thermal Conductivity Detector) and two FIDs (Flame Ionization Detector) during the reaction. The 13X molecular sieve packed column was used to separate C_2H_6 and N_2 in the outlet gas, and then those gases were detected by the TCD detector. In addition, the heavy aromatic products and low-carbon hydrocarbon products in the outlet gas were are separated by InertCap 1301 capillary column and Porapak Q packed column respectively, and then detected by two FID detectors. After the reaction, the spent catalysts were carefully cooled down to room temperature and then collected.

2.6 Calculation Method

10 vol% N_2 contained in the feed gas (C_2H_6/N_2, 9/1, v/v) was used as an internal standard to calculate the volume flow rate of the reactor outlet (F^{out}, mol/h, Eq. (1)), and then the ethane conversion and product selectivity were obtained basing on Eqs. (2) and (3).

$$F^{in} \times X^{in}_{N_2} = F^{out} \times X^{out}_{N_2} \quad (1)$$

$$\text{Conv.} = \frac{F^{in} \times X^{in}_{C_2H_6} - F^{out} \times X^{out}_{C_2H_6}}{F^{in} \times X^{in}_{C_2H_6}} \times 100\% \quad (2)$$

$$S_i = \frac{R_i}{F^{in} \times 2 \times X^{in}_{C_2H_6} \times \text{Conv.}} \times 100\% \quad (3)$$

Among this, X represents the mole fraction, and R_i represents the carbon mole of product i.

2.7 Catalyst Characterization

The XRD (X-ray diffraction) patterns were obtained using a Rigaku Ultima IV diffractometer with Cu Kα in the scan angle (2θ) range of 5 ~ 90°.

Quantachrome Autosorb iQ automated gas sorption analyzer was used to measure the physicochemical properties of the catalyst including BET surface area and pore volume through N_2 physical adsorption at 77 K.

The actual Si/Al ratio of HZSM-5 and actual metal content of the catalyst were obtained by XRF (X-ray fluorescence) measure through a PANalytical Axios spectrometer.

SEM and TEM images (including STEM images) of catalysts were obtained on a ZEISS G300 field-emission scanning electron microscope and JEM-2200FS transmission electron microscopy, respectively.

The UV-vis DRS (Diffuse reflectance ultraviolet-visible spectra) of catalysts were recorded with a Shimadzu UV-3600 spectrophotometer equipped with an integrating sphere. $BaSO_4$ was used as a reference material.

H_2-TPR (Temperature programmed reduction) of catalysts were performed on the Autochem II 2920 device with a TCD detector.

Normal and In-situ XPS (X-ray photoelectron spectroscopy) measurements were performed using a Kratos AXIS Supra spectrometer equipped with a monochromatic Al Kα radiation source. For in-situ XPS, due to the carbon deposit on catalyst, we etched the fresh and spent catalysts using polyatomic Ar_{n+}-clusters to accurately investigate the Zn species before and after the reaction. The sputtering time and sputtering depth are 60 s and 12 nm, respectively. The C 1s peak at 284.8 eV were used as a reference for calibration of binding energies.

In-situ DRIFTS (In-situ diffuse reflection Fourier transform infrared spectroscopy) of catalysts ranging from 4000 to 800 cm^{-1} (the optical resolution is 4 cm^{-1}) were obtained on a Bruker TENSOR 27 spectrometer, which equipped with an MCT narrowband detector. Meanwhile, the device is also equipped with a modified in-situ reaction cell with ZnSe windows and drying device.

For in-situ DRIFTS of the hydroxyl groups of catalysts, firstly, about 50 mg of the samples were carefully placed into the reaction cell. Then, the samples were heated in an N_2 flow (20 ml/min) at 200 °C for 30 min to remove the moisture and cooled to 30 °C in a pure N_2 stream. Finally, the hydroxyl vibration spectra were obtained by subtracting the background spectra (the background spectra were recorded with KBr as a reference at the same temperature of test) from the measured sample spectra at different temperatures.

For in-situ DRIFTS of ethane dehydrogenation, firstly, about 50 mg of the samples were carefully placed into the reaction cell and heated in an N_2 flow (20 ml/min) at 200 °C for 30 min to remove the moisture. Secondly, the samples were further heated to 250 °C in a pure N_2 stream. In this process, the background spectrum of catalysts under N_2 atmosphere was collected at 250 °C. Finally, the C_2H_6/N_2 (1/19, v/v, 20 ml/min) was introduced into the cell, and then the DRIFTS spectra were collected every 1 min during the in-situ reaction. For in-situ DRIFTS of C_2H_4 adsorbed on HZSM-5, the background spectrum was collected at 30 °C. Then, the C_2H_4/N_2 (1/19, v/v, 20 ml/min) was introduced into the cell for 10 min, and then gas flow was switched to a high purity N_2 stream at flow rate of 20 ml/min to purge the cell for 30 min. Finally, the DRIFTS spectra were collected.

For in-situ DRIFTS of toluene adsorbed on HZSM-5, the background spectrum was collected at 250 °C. Subsequently, toluene (5.03 kPa, 30 °C) previously placed in an ice-cold trap was blown into the reaction cell using pure N_2 at flow rate of 20 ml/min for 10 min, and then gas flow was switched to a high purity N_2 stream at flow rate of 20 ml/min to purge the reaction cell for 30 min. Finally, the DRIFTS spectra were obtained.

The acidic properties of the samples were analyzed by NH_3-TPD (Ammonia temperature-programmed desorption) obtained on a Quantachrome automated gas sorption analyzer and Py-IR (Pyridine adsorption infrared spectroscopy) abtained on the Thermo fisher Nicolet iS50 instrument.

The amount of coke in the spent catalysts were quantified using Shimadzu DTG-60 thermogravimetric analyzer.

^{27}Al MAS NMR spectra of the samples were recorded on a Bruker AV300 spectrometer (7.05 T) at a frequency of 104.3 MHz.

3 Results and Discussion

3.1 XRD and Physisorption

Figure 1 shows the XRD patterns of the fresh catalysts. Both Zn@HZSM-5 and Zn/HZSM-5 exhibit typical diffraction peaks corresponding to the typical MFI topological structure without diffraction peaks of ZnO, suggesting that Zn species are highly dispersed on the HZSM-5 and do not change

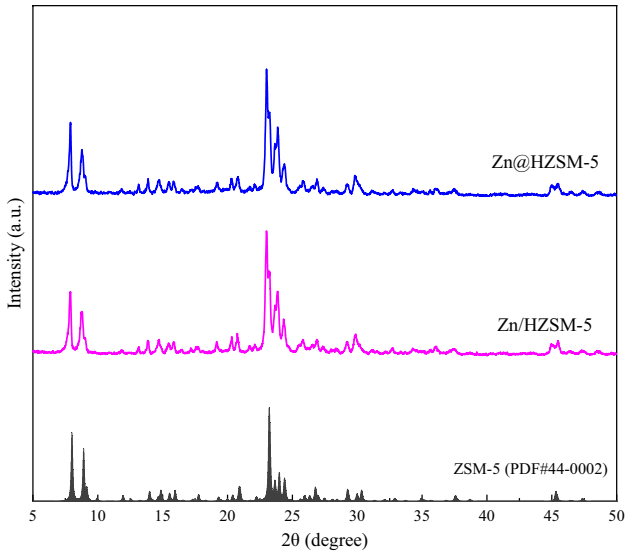

Fig. 1 XRD patterns of the Zn-based catalysts and pure HZSM-5

the zeolite crystal structure. As shown in Table 1, the BET surface area and micropore volume of conventional Zn/HZSM-5 (365 m^2/g, 0.15 cm^3/g) are lower than that of the embedded Zn@HZSM-5 (392 m^2/g, 0.16 cm^3/g) due to the blockage of the HZSM-5 channels by the Zn particles [7]. Combining with those results, we can reasonably conclude that the two-step crystallization method of the embedded Zn@HZSM-5 catalyst successfully synthesizes the typical ZSM-5 crystal structure and does not change the pore structure of HZSM-5. Additionally, the type I adsorption/desorption isotherm curve and the pore size distribution of about 0.50 nm indicate that samples are typical microporous HZSM-5 catalyst, as shown in Fig. S1.

3.2 SEM, TEM and XPS

The SEM images of the Zn@HZSM-5 in Fig. 2a and b exhibit a well-developed morphology of ZSM-5 with an octagonal shape and twin intergrowth crystals with a crystal size of 5 ~ 10 μm, indicating a relatively good uniformity and high crystallinity, which is consistent with XRD results.

The micromorphology and microstructure of Zn@HZSM-5 and Zn/HZSM-5 catalysts were characterized by TEM. As shown in Fig. 3b, some Zn species of Zn/HZSM-5 appear as large zinc oxide clusters. However, for Zn@HZSM-5 (Fig. 3a), smaller particle size in the form of zinc oxide is dispersed in HZSM-5 zeolite compared with Zn/HZSM-5, which is consistent with the result of the EDX elemental mappings of Zn@HZSM-5 in Fig. 2d and EDS spectrum in Fig. 2e and f. Meanwhile, the particle size of Zn species in Zn@HZSM-5 is closed to that of the precursor Zn/SiO_2 in Fig. S2, meaning that the two-step crystallization method does not change the particle size and the distribution of Zn species. Meanwhile, ZnO particles distributed throughout the newly formed HZSM-5 zeolite crystals, indicating the ZnO nanoparticles from Zn/SiO_2 precursor are well embedded inside the newly formed HZSM-5 crystal and not sintered during the hydrothermal synthesis and subsequent calcination process. As shown in Fig. 3d, a large amount of Zn species aggregates on the spent Zn/HZSM-5 was found after the reaction. The average particle size of Zn species in the spent Zn/HZSM-5 (15.4 nm) is larger than that in the fresh Zn/HZSM-5 (7.3 nm, Fig. 3b). On the contrary, the particle size of Zn species of the spent Zn@HZSM-5 catalyst (4.6 nm, Fig. 3c) does no increase in comparison to fresh Zn@HZSM-5 (4.4 nm, Fig. 3a), indicating that the Zn@HZSM-5 has excellent resistance to agglomeration due to its unique embedded structure. Meanwhile, as shown in Table 1, the Zn content (2.76 wt%) determined by etched in-situ XPS at 12 nm below the surface of the Zn@HZSM-5 catalyst is closer to the Zn content (2.79 wt%) determined by XRF, indicating that the Zn species are well embedded inside the HZSM-5. Moreover, the cross-sectional element distribution of the single crystal in Fig. 2f shows that the single crystal has a uniform distribution of Zn element. Meanwhile, the Si/Al ratio of Zn@HZSM-5 catalyst, determined by EDS and XRF, proves the zeolite is synthesized as designed.

The fresh catalysts were characterized by in-situ X-ray photoelectron spectroscopy (in-situ XPS). The results of normal in-situ XPS for two samples are shown in Fig. S3. It can be seen that there are very weak Zn signals from

Table 1 Physicochemical properties of the fresh catalysts

Sample	Zn content[a]		Si/Al[b]		S_{BET}	S_{micro}	S_{ext}	V_{total}	V_{micro}[c]	V_{meso}[d]
	XPS	XRF	EDS	XRF	(m^2/g)	(m^2/g)	(m^2/g)	(cm^3/g)	(cm^3/g)	(cm^3/g)
HZSM-5	—	—	—	21	425	379	45	0.22	0.17	0.05
Zn/HZSM-5	2.80	2.89	26	21	365	321	44	0.20	0.15	0.05
Zn@HZSM-5	2.76	2.79	27	20	392	359	33	0.19	0.16	0.03

[a]Zn content (wt%), bulk and surface Zn content determined by XRF and XPS

[b]Si/Al, the molar ratio of Si/Al determined by EDS and XRF

[c]V_{micro}, micropore volume determined by the t-plot method

[d]V_{meso}, mesopore volume determined by V_{total}–V_{micro}

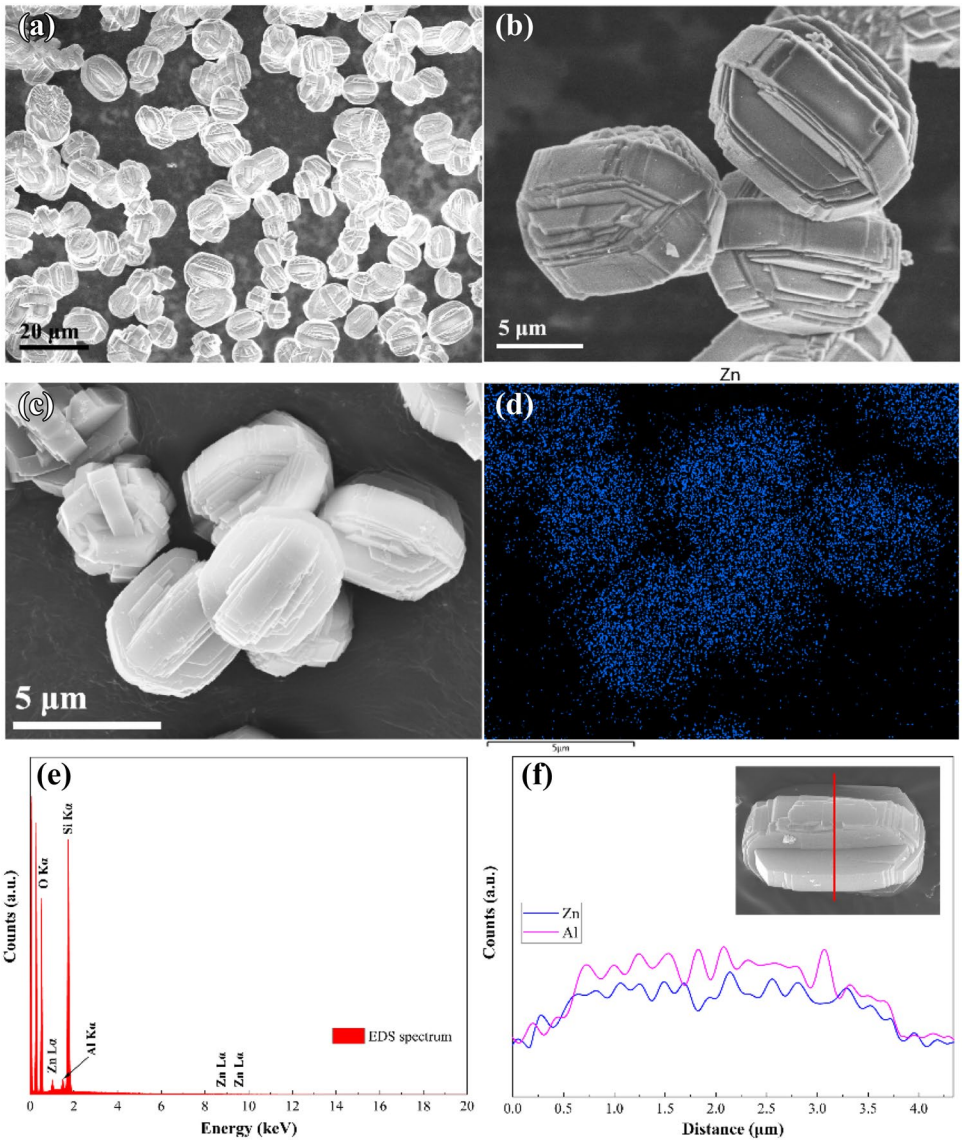

Fig. 2 The SEM image of the Zn@HZSM-5 (**a**, **b**, **c**). The EDX-mapping of Zn elemental (**d**). The EDS spectrum of Zn@HZSM-5 crystallites (**e**). The elemental line profiles along the red line (inset) of single crystal (**f**)

1020 to 1025 eV for fresh Zn@HZSM-5 catalyst, proving that most of the Zn particles of this catalyst did not locate on the outer surface of HZSM-5 but were embedded inside the zeolite crystal as designed. However, the Zn signals of Zn/HZSM-5 are relatively stronger than that of Zn@HZSM-5 because the conventional impregnation method could not avoid some Zn species locating on the outer surface of HZSM-5.

As illustrated in Scheme 1, it is considered that the zeolite frameworks were newly form by the dissolved Si species with the added TPAOH and Al species, which grow on the surface of the formerly formed ZnO nanoparticles on Zn/SiO_2 during hydrothermal synthesis, resulting in the formerly formed ZnO nanoparticles on Zn/SiO_2 are encapsulated inside newly formed HZSM-5 crystal.

3.3 *UV–Vis DRS and H_2-TPR*

The UV-vis DRS spectra of the Zn/HZSM-5 and Zn@HZSM-5 are shown in Fig. 4. For the Zn/HZSM-5 catalyst, two bands located at 220 nm and 240 nm species are designated to tightly combined with HZSM-5 and exist as framework bonded Zn species [19, 23], and there is a strong band at 360 nm, meaning that some Zn species are presented as ZnO particles or $[Zn–O–Zn]^{2+}$ clusters [24–26]. However, even though the ZnO particle size (dispersion) is almost same for two catalyst, the band at 361 nm of Zn@HZSM-5 is very weak peak than that of Zn/HZSM-5, indicating that there are very few $[Zn–O–Zn]^{2+}$ clusters in the Zn@HZSM-5 catalyst as proved by in-situ XPS. Meanwhile, compared with Zn@HZSM-5, the band at 240 nm is more

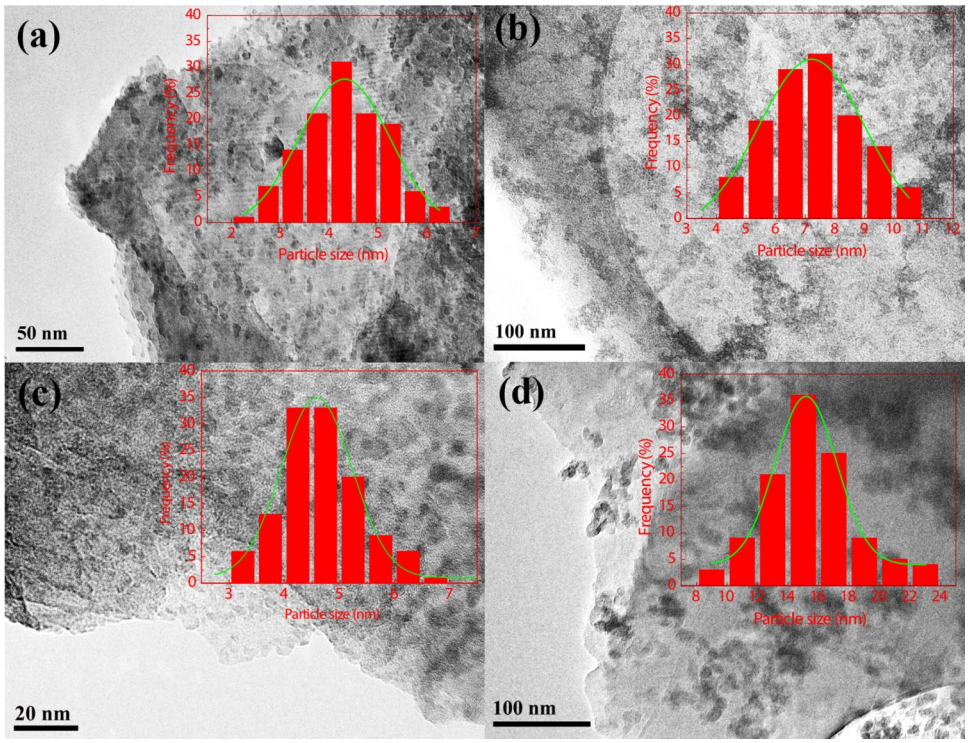

Fig. 3 The TEM images of fresh Zn@HZSM-5 (**a**), Zn/HZSM-5 (**b**) catalysts and the used Zn@HZSM-5 (**c**), Zn/HZSM-5 (**d**) catalysts

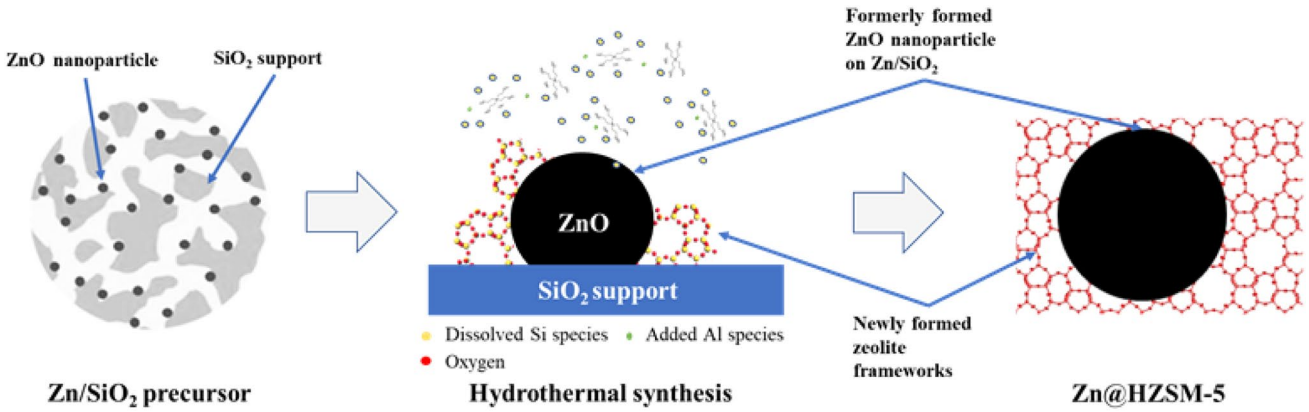

Scheme 1 Image of synthesis of the embedded Zn@HZSM-5

evident for Zn/HZSM-5 catalyst, indicating that the Zn species attached to the zeolite framework in different type for two catalysts. Based on those results, it is considered that for embedded Zn@HZSM-5 the newly formed zeolite frameworks grow on the surface of the formerly formed ZnO nanoparticles of Zn/SiO_2 precursor, leading to the different interaction of Zn species and zeolite frameworks resulting in weak bands at 240 nm and 360 nm.

The temperature-programmed reduction (H_2-TPR) profiles for Zn@HZSM-5 and Zn/HZSM-5 samples are shown in Fig. 5. For the Zn@HZSM-5 and Zn/HZSM-5, a reduction peak at ~ 80 °C is observed, which is attributed to the H_2 uptake due to heterolytic dissociation of H_2 [7, 12]. It is reported that $Zn(OH)^+$ species can promote the heterolytic dissociation of H_2 at low temperatures [12]. On the other hand, the $Zn(OH)^+$ species of the Zn-based HZSM-5 catalyst can react with H_2 to convert into ZnH^+ by dehydroxylation at about 300 °C [27]. Therefore, the reduction peak at ~ 310 °C should be associated with the dehydroxylation of $Zn(OH)^+$ species. For the Zn@HZSM-5 catalyst, the peak of the dehydroxylation of $Zn(OH)^+$ species is significantly stronger than that of Zn/HZSM-5, indicating that a large number of $Zn(OH)^+$ species exist on the Zn@HZSM-5 catalyst. Additionally, the TPR profile of pure ZnO powders exhibits a broad reduction peak at the rage of 400 ~ 750 °C in Fig. 5. Therefore, the reduction peak of Zn/HZSM-5 above 400 °C

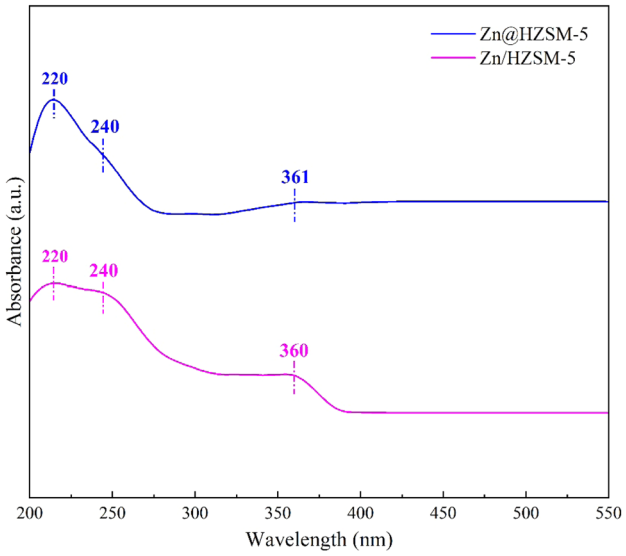

Fig. 4 The UV-vis DRS spectrum of the Zn@HZSM-5 and Zn/HZSM-5 catalysts

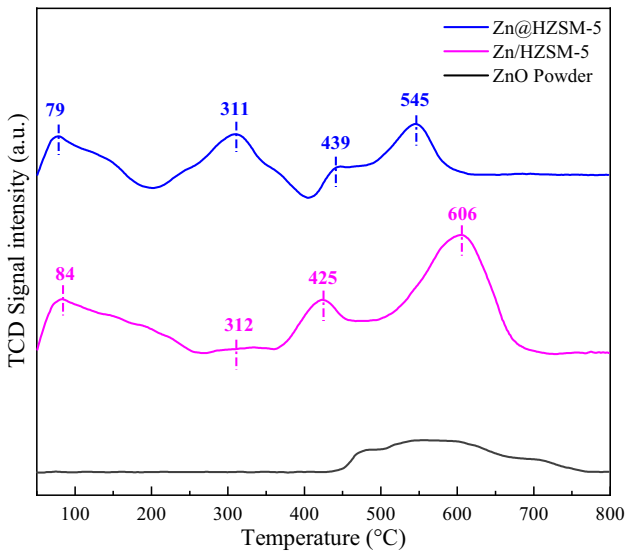

Fig. 5 The H_2-TPR profiles of the Zn-based catalysts and ZnO Powder

can be assigned to the reduction of bulk ZnO. Compared with Zn/HZSM-5, the different reduction peak location of Zn@HZSM-5 indicates the different interaction between Zn and HZSM-5 is formed due to the embedment structure.

3.4 Sputter Etching In-Situ XPS

In order to accurately investigate the Zn species located inside zeolite crystal, the samples were in-situ etched using sputter etching by polyatomic Ar_{n+}-clusters before collection of XPS signals, and sputter etching depth was 12 nm. As

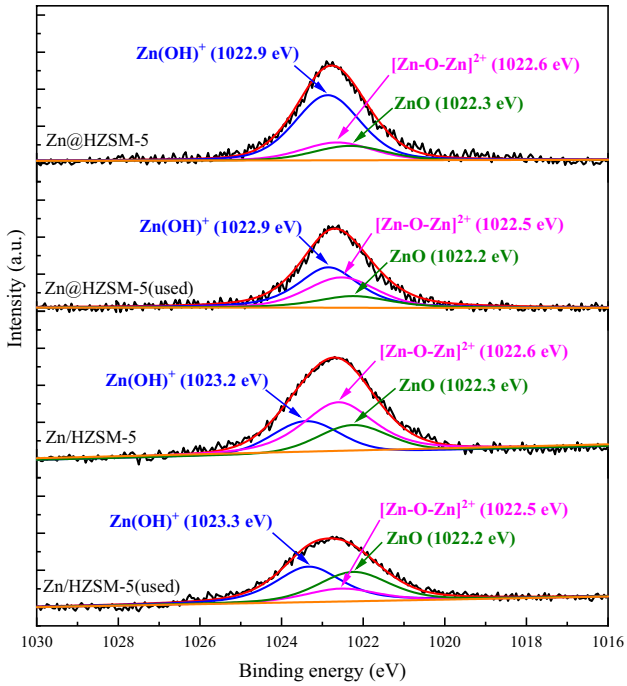

Fig. 6 The etched in-situ XPS spectra of the Zn@HZSM-5 and Zn/HZSM-5 catalysts before and after the reaction

shown in Fig. 6, after deconvolution of the XPS spectrum, several binding energy characteristic peaks were observed, indicating that there are different types of Zn species in the Zn-based HZSM-5. Considering the pure ZnO and ZnO on the Zn/SiO_2 show peaks at 1021.6 eV and 1022.3 eV in Fig. S4, respectively. The peak at ~ 1022.3 eV of the fresh Zn-based catalyst is reasonably attributed to the ZnO state species [28].

For Zn/HZSM-5, some Zn species exist in the micropores of HZSM-5 as small $(Zn_xO_y)_n$ clusters, and others were interacted with the intrinsic proton acidic sites in HZSM-5 to form $Zn(OH)^+$ species, and some $Zn(OH)^+$ groups would form $[Zn–O–Zn]^{2+}$ or small clusters of zinc oxide in the micropores [26]. Therefore, the peak at 1023.2 eV and 1022.6 eV for Zn/HZSM-5 can be ascribed to $Zn(OH)^+$ and $[Zn–O–Zn]^{2+}$ species, respectively [29, 30]. For Zn@HZSM-5, as shown in Fig. 6 and Table S1, the Zn species in fresh Zn@HZSM-5 are mainly $Zn(OH)^+$ species, accounting for 65.5%. The proportion of ZnO species and $[Zn–O–Zn]^{2+}$ species are only 15.2% and 19.3%, respectively. However, for fresh Zn/HZSM-5, 51.6% of Zn species exist as $[Zn–O–Zn]^{2+}$, meanwhile the $Zn(OH)^+$ and ZnO species are 25.4% and 23.0%, respectively. Because the $[Zn–O–Zn]^{2+}$ species prepared by impregnation method are easy to be aggregated to form $(Zn_xO_y)_n$ clusters at high reaction temperature [26], as proved by TEM images, for Zn/HZSM-5 after 10 h of reaction, the content of $[Zn–O–Zn]^{2+}$ species decrease to 20.3%, and the ZnO state species increase from

23.0 to 35.9%; meanwhile, the $Zn(OH)^+$ species increase to 43.8%. For Zn@HZSM-5 after 35 h reaction, it is found that the content of $[Zn–O–Zn]^{2+}$ species increase to 36.3%, and the ZnO species slightly increase to 16.3%. Meanwhile, the $Zn(OH)^+$ species for the spent Zn@HZSM-5 catalyst decrease to 47.4%, compared with the fresh Zn@HZSM-5.

3.5 In-Situ DRIFTS Spectra of Hydroxyl Groups

The DRIFTS spectra of the OH groups on the catalysts can offer more information about the acidic properties. Figure 7 shows the in-situ DRIFTS spectra of the hydroxyl groups on pure HZSM-5 and the Zn-based HZSM-5 catalysts at 30 °C, which were obtained by subtracting the background spectra, and the background spectra were recorded using KBr at same temperature of test. Typically, the band at ~ 3740 cm^{-1} belongs to an isolated external silanol (Si–OH), and the band at ~ 3660 cm^{-1} is associated with the extra-framework Al species, while the band at ~ 3610 cm^{-1} belongs to the bridging acidic hydroxyl group (Si(OH)Al) [13, 31]. The broadband at 3400 ~ 3550 cm^{-1} is attributed to the delocalized hydrogen-bonded groups of lattice defects [32].

It is worth noting that the Zn@HZSM-5 catalyst exhibits three new bands at about ~ 3630, ~ 3680, and ~ 3725 cm^{-1}. The band at ~ 3630 cm^{-1} is attributed to Si-OH nest [33], and the band at ~ 3725 cm^{-1} corresponds to free internal silanol (Si–OH) [13, 32]. The band at ~ 3680 cm^{-1} is attributed to $Zn(OH)^+$ groups in zeolites [32, 34, 35], and the $Zn(OH)^+$ groups of Zn@HZSM-5 are very stable and do not change with increasing temperature, as shown in Fig. 7a. In general, the introduction of metals usually results in a decrease in the strength of the band of the free internal silanol (Si–OH) [10]. However, Zn@HZSM-5 shows a distinct band attributed to the free internal silanol (~ 3725 cm^{-1}) and even a band assigned to Si–OH nest (~ 3630 cm^{-1}) in Fig. 7a, suggesting that these silanol groups do not interact with the $Zn(OH)^+$ to form of ZO-Zn–O–Si species due to the specific embedment structure [10]. On the other hand, as shown in Fig. 7b, the Zn/HZSM-5 did not show the bands attributed to $(ZnOH)^+$ groups (~ 3680 cm^{-1}) at both room temperature or high temperatures, suggesting that the content of $Zn(OH)^+$ species is very few in Zn/HZSM-5. These results indicate that the embedment of Zn@HZSM-5 catalyst, prepared by the two-step crystallization method, has a significant effect on the distribution of the hydroxyl group due to the unique introduction method of Zn species, which would further influence the stability and selectivity of the catalyst in ethane dehydrogenation.

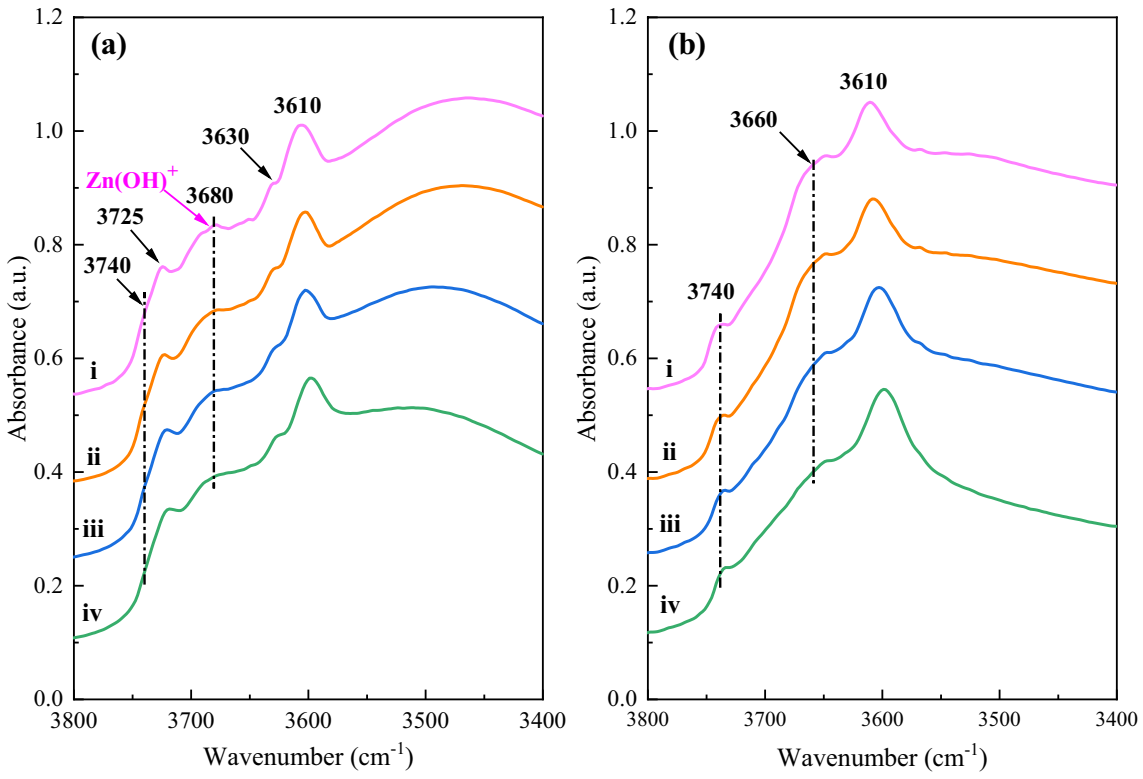

Fig. 7 The in-situ DRIFTS spectra of hydroxyl groups of Zn@HZSM-5 (**a**) and Zn/HZSM-5 (**b**) at different temperatures. (i) 30 °C, (ii) 100 °C, (iii) 200 °C, (iv) 300 °C

3.6 Catalytic Tests

The reaction performance of ethane dehydrogenation over Zn@HZSM-5 and Zn/HZSM-5 catalysts with time on stream are shown in Fig. 8 and Table 2. The conversion of Zn/HZSM-5 decreased rapidly from 22.1 to 0.5% within 10 h reaction. Moreover, the selectivity of aromatics over Zn/HZSM-5 declined sharply from 47.7 to 16.9%, while the selectivity of ethylene increased quickly from 16.9 to 78.4%. However, for the Zn@HZSM-5, the conversion of ethane only slightly decreases from 14.5 to 14.3%. Meanwhile, the selectivity of the ethylene reduces from 74.4 to 42.8%, and the selectivity of the aromatics increases from 22.6 to 43.6% during 10 h reaction.

It is well known that coke deposits are the main reason for acidic zeolite catalysts deactivation since coke could cover and reduce the active metal species and the acidic sites. There are two kinds of coke formation in the Zn-based HZSM-5 catalyst. One is directly from the deep dehydrogenation of ethane formed on the Zn species leading to form undesired methane; another coke is formed from the aromatic products [18]. Therefore, CH_4 can be used as one of the indicators of coke formation. The initial CH_4 selectivity of Zn@HZSM-5 is only 1.5%, which is much lower than that of Zn/HZSM-5 (27.9%) as compared in Fig. 8, indicating that Zn@HZSM-5 is more difficult to form coke from the deep dehydrogenation of ethane. As shown in Fig. 8, for the Zn/HZSM-5, the selectivity of aromatics rapidly decreased, indicating the formation of coke from polyaromatic hydrocarbons (PAHs). Therefore, it is believed that the main reason for the severe deactivation of Zn/HZSM-5 is the Zn active species and the acidic site of HZSM-5 are covered by the formed coke. On the contrary, for Zn@HZSM-5, the selectivity of aromatics is increasing during 10 h reaction

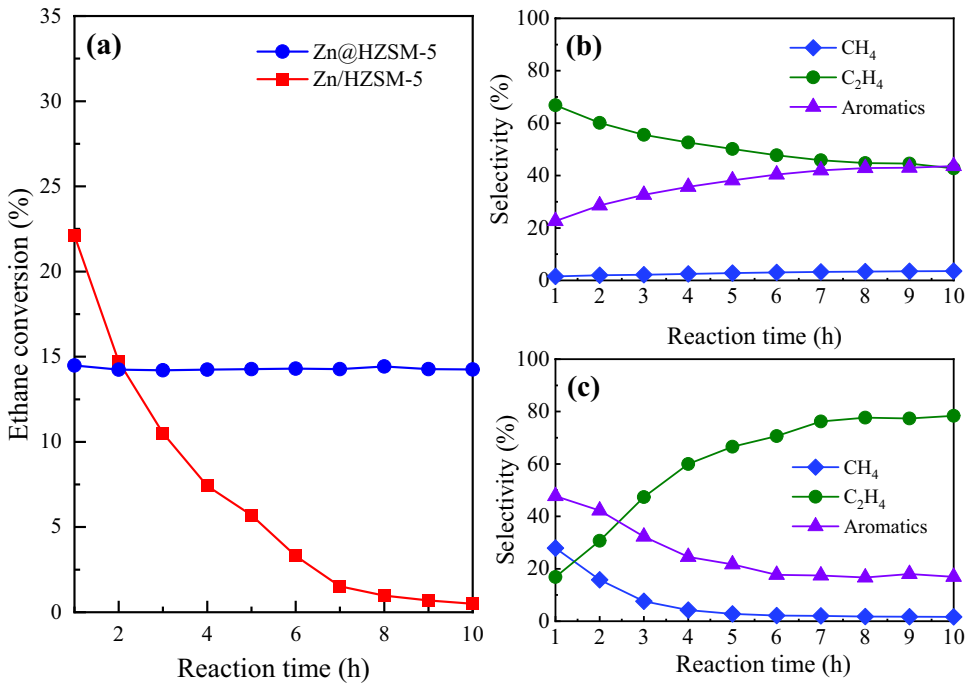

Fig. 8 TOS of Zn-based catalysts (**a**). The product distribution of Zn@HZSM-5 (**b**) and Zn/HZSM-5 (**c**). Reaction conditions: 550 °C, 0.1 MPa, 2000 mL $h^{-1}{\cdot}g^{-1}$, $C_2H_6/N_2=9$

Table 2 Reaction performance of Zn-based catalysts[a]

Reaction	Conversion[b]/%	Selectivity[c]/%								
		CH_4	$C_2^=$	$C_{3\text{-}5}$[d]	C_6	C_7	C_8	C_9	C_{9+}	Aromatics[e]
Zn/HZSM-5(10 h)	0.49	1.67	78.39	3.02	0.93	0.33	0.06	0.11	15.50	16.91
Zn@HZSM-5(10 h)	14.25	3.57	42.75	10.05	16.36	15.59	2.53	1.23	7.92	43.63
Zn@HZSM-5(35 h)	13.40	2.76	51.07	10.57	12.63	12.13	2.88	1.19	6.77	35.60

[a]Reaction condition: 0.3 g catalyst; GHSV = 2000 mL $h^{-1}{\cdot}g^{-1}$; T = 550 ℃; P = 0.1 MPa; $C_2H_6/N_2=9$

[b]Conversion was calculated by TCD data

[c]Selectivity of products were calculated from FID analysis

[d]Including C_{3-5} alkanes and alkene

[e]Including C_6 and C_{6+} aromatics

(Fig. 8b). Furthermore, the selectivity of undesired CH_4 was only 3.6% after 10 h reaction. The quite different reaction performance indicates the different properties of active phase and acidic sites between the two catalysts.

The stability of the catalyst was investigated to evaluate the catalytic performance of Zn@HZSM-5 further, as shown in Fig. 9. It can be seen that the catalyst maintains excellent stability in 35 h of reaction time, and the final conversion is very closed to the initial conversion. Moreover, the selectivity of desired products (ethylene + aromatics) remained at 86.7%, and the selectivity of by-product CH_4 was 2.8%, respectively, after 35 h of reaction.

3.7 Operando DRIFTS of Ethane Aromatization Reaction

To further understand the properties of different catalysts, the EDA reaction was monitored over fresh Zn@HZSM-5 and Zn/HZSM-5 catalysts using in situ diffuse reflectance infrared fourier transform spectroscopy (DRIFTS). Ethane (5% in nitrogen) feed gas was introduced into an in-situ cell at 250 ℃ and then tracked with DRIFTS, which was obtained by subtracting the background spectra, and the background spectra were recorded using catalyst under N_2 flow at the same temperature. As shown in Fig. 10, Fig. S5 and Fig. S6. The strong broadbands ranging from 2800 to 3100 cm^{-1} can be assigned to the C–H stretching vibrations of the CH_3 and CH_2 groups, and those of δ bending vibrations appear at 1425–1485 cm^{-1} [36]. It is believed that those CH_3 and CH_2 groups should be from gas-phase ethane and ethane molecules adsorption inside the zeolite channels and on the supported metal species [37], as

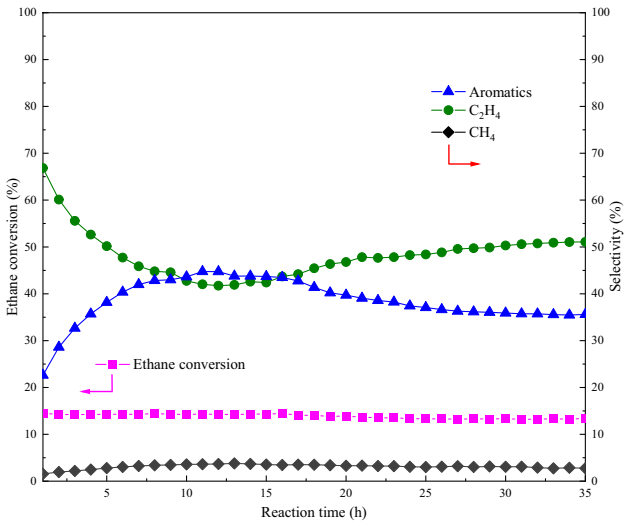

Fig. 9 The Stability and the product distribution of Zn@HZSM-5 catalyst. Reaction conditions: 550 °C, 0.1 MPa, 2000 mL $h^{-1}{\cdot}g^{-1}$, $C_2H_6/N_2 = 9$

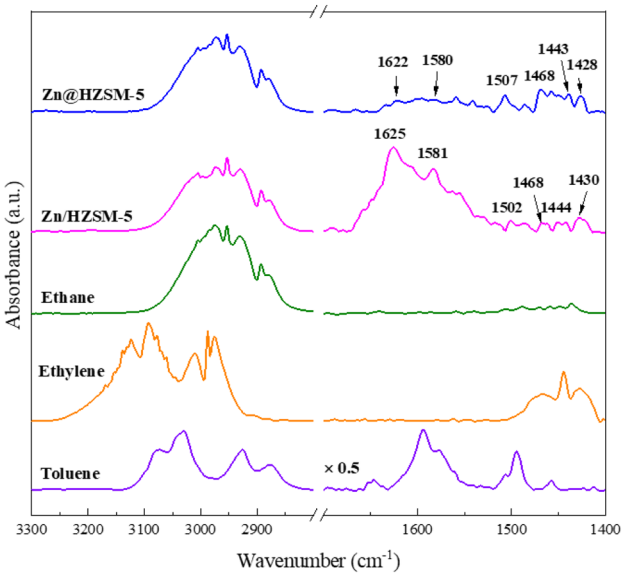

Fig. 10 The in-situ DRIFTS spectra of ethane adsorbed on Zn-based catalysts. The operating temperature except for C_2H_4, which is 30 °C, the other operating temperatures are 250 °C. The in-situ DRIFTS spectra of reference substances (gas phase), including C_2H_4, C_2H_6, and toluene (C_7H_8) were recorded on the pure HZSM-5 (Si/Al = 20) after adsorbed for 10 min. The in-situ DRIFTS spectra of Zn/HZSM-5 and Zn@HZSM-5 were recorded after switching to ethane for 20 min

well as hydrocarbon products of EDA reaction. As shown in Fig. 10, several strong broadbands are observed on the Zn/HZSM-5 catalyst from 1500 to 1680 cm^{-1}. As reported by kinds of literature, broadband centered near 1590 cm^{-1} suggests the formation of polyaromatic hydrocarbon species [36, 38]. Comparing to the IR spectra of toluene (Fig. 10), it is believed that many kinds of aromatics are formed on the Zn/HZSM-5 catalyst, resulting in complex adsorption bands in the range of 1500–1680 cm^{-1} [39]. For Zn/HZSM-5 (Fig. S5b), the intensity of the broadband centered at ~ 1625 cm^{-1} attributed to the aromatics increased rapidly as the reaction progressed, which supports the conclusion that Zn/HZSM-5 has high initial ethane conversion and aromatic selectivity. Moreover, the sharp shoulder band centered at ~ 1581 cm^{-1} belonging to cyclic-enyl carbenium ions, which are precursors of aromatic carbocations [40, 41], also becomes more and more apparent, indicating that more ethane is converted into heavy aromatics as the reaction time increases.

For Zn@HZSM-5, there are several very week bands located at a range of 1500–1680 cm^{-1}, suggesting the less formation of aromatics products during EDA reaction on this catalyst. During the reaction (Fig. S5a), the intensity of the weak broadband centered at ~ 1622 cm^{-1} increased slightly, suggesting only a small amount of aromatics are formed during the initial stage of the reaction on this catalyst. Meanwhile, the intensity of the band centered at ~ 1580 cm^{-1} did

not change obviously, indicating that few precursors of aromatic carbocations are formed, which is also powerful evidence to support the reaction results of Zn@HZSM-5. Therefore, from the results of operando DRIFTS, it is believed that the Zn@HZSM-5 catalyst is moderate to forming aromatics, contributing to remarkable stability during the ethane aromatization reaction.

Besides, an interesting phenomenon was observed in the operando DRIFTS spectra of the hydroxyl groups on Zn/HZSM-5 and Zn@HZSM-5 catalysts during the ethane aromatization at 250 ℃ Concerning Fig. 7, it can be seen that the increased temperature induces the red-shifted the isolated external silanol bands and the bridging acidic hydroxyl group bands. Therefore, as shown in Fig. S6, bands of $Zn(OH)^+$ species also shifts to a lower wavenumber. The absorption peak of Zn/HZSM-5 catalyst (Fig. S6b) centered at ~ 3666 cm^{-1} could be attributed to $Zn(OH)^+$ species, and the intensity of this band increases rapidly, indicating that a large number of $Zn(OH)^+$ species are formed in Zn/HZSM-5 during the reaction. However, for the Zn@HZSM-5 catalyst (Fig. S6a), the bands of the isolated external silanol (3730 cm^{-1}) and free internal silanol (3704 cm^{-1}) are slightly formed, and the change of the $Zn(OH)^+$ species cannot be detected. These results are consistent with results of in-situ XPS, suggesting that the different Zn species dynamically transform and strongly influence the selectivity and stability of ethane aromatization catalysts. According to literature [26, 42], C–H bonds of ethane can be activated by oxygen-bridged zinc sites, and the bridging oxygen in $[Zn–O–Zn]^{2+}$ can abstract the hydrogen in the C–H bond to form $Zn(OH)^+$ species, and eventually ethylene is released. Therefore, in this study, due to the Zn/HZSM-5 catalyst contains a large amount of $[Zn–O–Zn]^{2+}$ species, the $[Zn–O–Zn]^{2+}$ species are transformed into $Zn(OH)^+$ species during the reaction, making the absorption peak attributed to $Zn(OH)^+$ species (Fig. S6) increase rapidly, as illustrated by in-situ XPS.

3.8 *NH_3-TPD, Py-FTIR and TGA*

The acidic properties of the samples were investigated by NH_3-TPD and Py-FTIR, as shown in Fig. 11 and Table S2. The desorption peaks of Zn/HZSM-5 changed drastically, indicating that the introduction of Zn has a significant effect on the acid strength and distribution of support HZSM-5. For Zn/HZSM-5 after a 10 h of reaction, the NH_3-TPD peaks decreased sharply because of the heavy coke deposits on the acid site and channel of the catalyst. In contrast, Zn@HZSM-5 after a 35 h of reaction, the NH_3-TPD curve has a small change and still retains a large number of acidic sites, which indicates that the catalyst has excellent resistance to coke deposits.

The pyridine adsorption FT-IR spectroscopy was operated to identify the types of acid sites over catalysts. As shown in Fig. 11b, the band centered at ~ 1454 cm^{-1} and ~ 1543 cm^{-1} are the vibrations of pyL and pyH^+ derived from the interaction of pyridine with Lewis (L) acid and Brønsted acid, respectively [43]. As compared in Fig. 11b, the Lewis acid

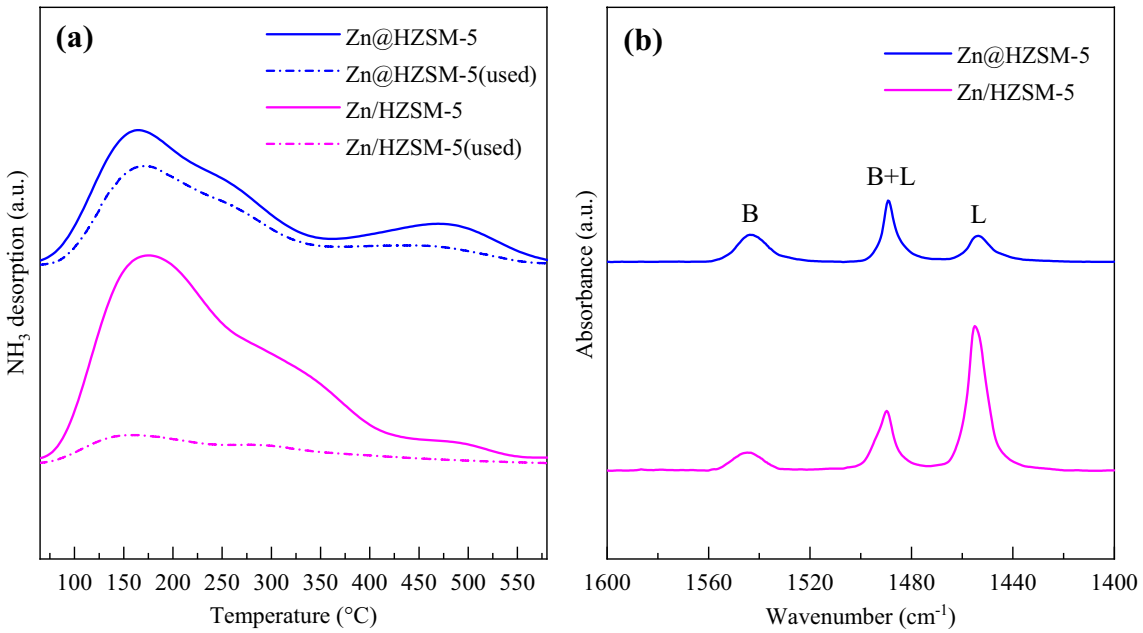

Fig. 11 NH_3-TPD profiles (**a**) and Py-FTIR spectra (**b**) desorbed at 150 °C of Zn-based HZSM-5 catalysts. (note the blue dashed line is the spent Zn@HZSM-5 (35 h), the red dashed line is the used Zn/HZSM-5 (10 h))

sites in Zn/HZSM-5 increased sharply than that of Zn@HZSM-5, indicating that impregnation of Zn species into HZSM-5 forms new Lewis acid sites resulting in higher initial selectivity of aromatics as shown in Fig. 8, contributing to fast deactivation due to PAHs formation [3].

To further investigate the nature and amount of coke formed in spent catalysts, TGA was applied and is discussed next. The TG analysis of used Zn-based HZSM-5 was shown in Fig. S7. The initial weight loss at a temperature below 250 °C, ascribed to the desorption of adsorbed water, and the weight loss above 250 °C is attributed to the combustion of coke. For the Zn/HZSM-5, the amount of coke was 8.26 wt% after 10 h of reaction, and the coke formation rate was 9.01 mg C/(g_{cat}·h). For Zn@HZSM-5, the amount of coke is only 2.39 wt% after 35 h reaction, which is much smaller than that of Zn/HZSM-5. Moreover, the coke formation rate for Zn@HZSM-5 is only 0.70 mg C/(g_{cat}·h), and the coke formation rate of Zn/HZSM-5 is nearly 13 times than that of Zn@HZSM-5. All those results indicate that the Zn@HZSM-5 has excellent resistance to coke deposits.

3.9 Discussion

It can be seen from Fig. S8 that the Zn/HZSM-5 (synthesis) catalyst has very similar reaction performance to Zn/HZSM-5 catalyst during ethane aromatization. Therefore, it is considered that using commercial HZSM-5 to prepared Zn/HZSM-5 catalyst would not influence the comparison the embedded Zn@HZSM-5 catalyst and conventional Zn/ZSM-5 catalyst.

The various characterization results suggest that the Zn@HZSM-5 catalyst has typical zeolite morphology and Zn species are embedded inside zeolite crystal, as proved by XRD, SEM and TEM. Meanwhile, as illustrated in Fig. 5 and Fig. S3, the Zn species of Zn@HZSM-5 only can be clearly detected by XPS after the samples were in-situ sputter etched for 12 nm from the outer surface, which further suggests the most Zn species are located inside HZSM-5 crystal but on the outer surface of the zeolite. Furthermore, the results of H_2-TPR and the etching XPS further prove that the Zn species on Zn@HZSM-5 catalyst are quite different from that on conventional Zn/HZSM-5 catalyst because of embedment structure. Besides, the Py-FTIR profile of Zn/HZSM-5 exhibits strong Lewis acid sites than that of Zn@HZSM-5 due to the impregnation of Zn species into HZSM-5 [3], suggesting the quite different structure between the two kind of catalysts.

In this study, the embedded catalyst is synthesized in-situ by a two-step crystallization method with Zn/SiO_2 precursor, as shown in Scheme 1. In this process, the formerly formed ZnO nanoparticles on Zn/SiO_2 are encapsulated by the newly formed zeolite framework. Namely, the newly formed zeolite frameworks grow on the surface of the formerly formed ZnO nanoparticles. Therefore, the connection or interaction between ZnO species and zeolite on Zn@HZSM-5 is different to the conventional Zn/HZSM-5, as illustrate by UV-vis DRS results. It is considered that the embedment structure of Zn@HZSM-5 adjusts the electronic state of Zn species, as proved by in-situ XPS, contributing to form more $Zn(OH)^+$ species, as confirmed by H_2-TPR, in-situ DRIFTS and in-situ XPS.

Furthermore, it is found that $Zn(OH)^+$ and $[Zn–O–Zn]^{2+}$ species are active sites for ethane aromatization for zinc based catalysts, and their dynamic transition significantly changes the reaction performance of ethane dehydrogenation. For the Zn/HZSM-5 catalyst, the existence of a large number of $[Zn–O–Zn]^{2+}$ species, as proved by UV-vis DRS and in-situ etching XPS, causes higher initial ethane conversion and higher selectivity of aromatics, as illustrated by operando DRIFTS of ethane aromatization reaction, resulting in large amount of coke deposits. However, $[Zn–O–Zn]^{2+}$ species on the Zn/HZSM-5 catalyst fast transit to $Zn(OH)^+$ species and subsequently form the sintered ZnO species during the reaction as confirmed by operando DRIFTS and in-situ etching XPS, leading to rapid deactivation. For the Zn@HZSM-5 catalyst, the embedded structure contributes to forming more $Zn(OH)^+$ species and delays the transformation of the $Zn(OH)^+$ species to $[Zn–O–Zn]^{2+}$ species, resulting in slowly increased selectivity of aromatics during the reaction. Therefore, the Zn@HZSM-5 catalyst realizes stable ethane conversion with dynamic selectivity.

4 Conclusion

In summary, the embedded Zn@HZSM-5 catalyst for ethane dehydrogenation to ethylene and aromatics has been successfully synthesized by a two-step crystallization process using Zn/SiO_2 precursor.

Due to this unique embedded structure, a large number of stable $Zn(OH)^+$ species are formed on the Zn@HZSM-5 catalyst, and those $Zn(OH)^+$ species have lower dehydrogenation activity than $[Zn–O–Zn]^{2+}$ species on conventional Zn/HZSM-5 catalyst, reducing the formation of undesired CH_4 and coke from deep dehydrogenation of ethane and the formed aromatics. Meanwhile, the dynamic transition of Zn species strongly affects the activity and selectivity of ethane dehydrogenation. The slow transform of Zn species on Zn@HZSM-5 catalyst contributes to stable ethane conversion with dynamic selectivity.

Supplementary Information The online version contains supplementary material available at https://doi.org/10.1007/s10562-021-03726-1.

Acknowledgements This work was supported by National Natural Science Foundation of People's Republic of China (Grant Nos. U20B2022), and Bingtuan Science and Technology Program

(2018BC008 and 2021DB006). This work was also supported by CNOOC.

Declarations

Conflict of interests The authors declare no competing financial interest.

References

1. Ma L, Zou X (2019) Appl Catal B 243:703–710
2. Li Q, He P, Jarvis J, Bhattacharya A, Mao X, Wang A, Bernard GM, Michaelis VK, Zeng H, Liu L, Song H (2018) Appl Catal B 236:13–24
3. Gao J, Wei C, Dong M, Wang G, Li Z, Qin Z, Wang J, Fan W (2019) ChemCatChem 11:3892–3902
4. Biscardi JA, Meitzner GD, Iglesia E (1998) J Catal 179:192–202
5. Albarracin-Suazo SC, Pagan-Torres YJ, Curet-Arana MC (2019) J Phys Chem C 123:16164–16171
6. Aleksandrov HA, Vayssilov GN, Rosch N (2006) J Mol Catal A Chem 256:149–155
7. Almutairi SMT, Mezari B, Magusin PCMM, Pidko EA, Hensen EJM (2011) ACS Catal 2:71–83
8. Schweitzer NM, Hu B, Das U, Kim H, Greeley J, Curtiss LA, Stair PC, Miller JT, Hock AS (2014) ACS Catal 4:1091–1098
9. Gabrienko AA, Arzumanov SS, Toktarev AV, Danilova IG, Prosvirin IP, Kriventsov VV, Zaikovskii VI, Freude D, Stepanov AG (2017) ACS Catal 7:1818–1830
10. Niu X, Gao J, Miao Q, Dong M, Wang G, Fan W, Qin Z, Wang J (2014) Microporous Mesoporous Mater 197:252–261
11. Zhang Y, Wu S, Xu X, Jiang H (2020) Catal Sci Technol 10:835–843
12. Song C, Li X, Zhu X, Liu S, Chen F, Liu F, Xu L (2016) Appl Catal A 519:48–55
13. Liu J, He N, Zhou W, Lin L, Liu G, Liu C, Wang J, Xin Q, Xiong G, Guo H (2018) Catal Sci Technol 8:4018–4029
14. Liu G, Liu J, He N, Miao C, Wang J, Xin Q, Guo H (2018) RSC Adv 8:18663–18671
15. Zhou W, Liu J, Wang J, Lin L, Zhang X, He N, Liu C, Guo H (2019) Catal Lett 149:2064–2077
16. Berndt H, Lietz G, Lucke B, Volter J (1996) Appl Catal A 146:351–363
17. Berndt H, Lietz G, Volter J (1996) Appl Catal A 146:365–379
18. Xiang Y, Wang H, Cheng J, Matsubu J (2018) Catal Sci Technol 8:1500–1516
19. Saito H, Inagaki S, Kojima K, Han Q, Yabe T, Ogo S, Kubota Y, Sekine Y (2018) Appl Catal A 549:76–81
20. Mehdad A, Gould NS, Xu B, Lobo RF (2018) Catal Sci Technol 8:358–366
21. Steinberg K, Mroczek U, Roessner F (1990) Appl Catal 66:37–44
22. Liu J, Chen J, Zhang Y (2013) Catal Sci Technol 3:2559–2564
23. Qi G, Wang Q, Xu J, Trébosc J, Lafon O, Wang C, Amoureux JP, Deng F (2016) Angew Chem Int Ed 55:15826–15830
24. Yu L, Huang S, Zhang S, Liu Z, Xin W, Xie S, Xu L (2012) ACS Catal 2:1203–1210
25. Xu J, Zheng A, Wang X, Qi G, Su J, Du J, Gan Z, Wu J, Wang W, Deng F (2012) Chem Sci 3:2932–2940
26. Mehdad A, Lobo RF (2017) Catal Sci Technol 7:3562–3572
27. Tamiyakul S, Sooknoi T, Lobban LL, Jongpatiwut S (2016) Appl Catal A 525:190–196
28. Li J, Gong Q, Liu Y, Kang R, Yang C, Qiu M, Hu Z, Zhu Z (2019) ChemCatChem 11:4755–4764
29. Wang K, Dong M, Niu X, Li J, Qin Z, Fan W, Wang J (2018) Catal Sci Technol 8:5646–5656
30. Zhang C, Kwak G, Lee YJ, Jun KW, Gao R, Park HG, Kim S, Min JE, Kang SC, Guan G (2019) Microporous Mesoporous Mater 284:316–326
31. Cairon O, Thomas K, Chambellan A, Chevreau T (2003) Appl Catal A 238:167–183
32. Kolyagin Y, Ordomsky V, Khimyak Y, Rebrov A, Fajula F, Ivanova I (2006) J Catal 238:122–133
33. Halasz I, Agarwal M, Marcus B, Cormier WE (2005) Microporous Mesoporous Mater 84:318–331
34. Wang F, Xiao W, Gao L, Xiao G (2016) Catal Sci Technol 6:3074–3086
35. Murray DK, Howard T, Goguen PW, Krawietz TR, Haw JF (1994) J Am Chem Soc 116:6354–6360
36. He Y, Song Y, Laursen S (2019) ACS Catal 9:10464–10468
37. Pidko E, Kazansky V (2005) Phys Chem Chem Phys 7:1939–1944
38. Liu G, Zhao Z, Wu T, Zeng L, Gong J (2016) ACS Catal 6:5207–5214
39. Miyata H, Ohno T, Hatayama F (1995) J Chem Soc Faraday Trans 91:3505–3510
40. Tabor E, Bernauer M, Wichterlova B, Dedecek J (2019) Catal Sci Technol 9:4262–4275
41. Shi S, Wu Y, Zhang M, Wei R, Gao L, Xiao G (2021) Mole Catal 509:111659
42. Barbosa LAMM, van Santen RA (2003) J Phys Chem B 107:14342–14349
43. Pan D, Xu S, Miao Y, Xu N, Wang H, Song X, Gao L, Xiao G (2019) Catal Sci Technol 9:739–752